doi: 10.1016/j.clay.2020.105678

Title: Mechanical strength and cationic dye adsorption ability of metakaolin-based geopolymer spheres

Authors: Valentina Medri[a*], Elettra Papa[a], Matteo Mor[a], Angelo Vaccari[a, b], Annalisa Natali Murri[a], Lucie Piotte[c], Cesare Melandri[a], Elena Landi[a]

[a] National Research Council of Italy, Institute of Science and Technology for Ceramics (CNR-ISTEC), Via Granarolo 64, 48018 Faenza, RA, Italy

[b] "Toso Montanari" Department of Industrial Chemistry, University of Bologna, 40100 Bologna, Italy.

[c] Faculté des Sciences & Techniques de Limoges, University of Limoges, 87000 Limoges, France.

***Corresponding Author**

Valentina Medri

Tel: +39 0546 699751

Fax: +39 0546 699799

e-mail: valentina.medri@istec.cnr.it

Abstract:

Metakaolin-based geopolymer spheres shaped by three different dripping techniques were investigated in terms of compressive strength and dye adsorption ability. Spheres were produced by injection and solidification in polyethylene glycol (PEG) or liquid nitrogen (ice-templating) and ionotropic gelation (alginate in calcium chloride). Mechanical tests by ISO 18591 evidenced that compressive strength was strictly linked to porosity and composition of the spheres, being 12.9 MPa with 29% of porosity for spheres produced in PEG, 2.1 MPa with a porosity of 64% for spheres shaped in liquid nitrogen and up to 19.6 MPa with a porosity of 59% for hybrid spheres with a skeleton of Ca-alginate. The influence of contact time and initial concentration on a cationic dye (methylene blue) adsorption was studied. Removal efficiency was related to morphology, porosity and specific surface area: after 24 h the percentage of adsorption was 94-98% for spheres

shaped in liquid nitrogen while below 75% for hybrid spheres and spheres produced in PEG. By adding TiO_2 P25 as photocatalytic phase to the hybrid spheres, an increase of removal efficiency of 33% was observed after 90 minutes under UV irradiation.

Keywords: Geopolymer spheres; injection-solidification; ionotropic gelation; mechanical strength; methylene blue; dye adsorption.

1. Introduction

The chemical species in watercourses are object of increasing attention because of their harmful impact on the environment. One of the major causes of environmental pollution derives from textile factories, as textile wastewater contains dyes mixed with various contaminants (Pereira et al., 2012; Rawat et al., 2016; Yaseen et al., 2019). The reference literature lists many methodologies for dyes removal from water, such as ion-exchange (Boyd et al., 1947; Wu et al., 2008; Liu et al., 2007; Zhou et al., 2019), chemical precipitation (Tan et al. 2000; Shen et al, 2019), membrane filtration (Kim et al, 2005; Ahmad et al, 2019), electrochemical treatment techniques (Körbahti, 2007). Among these, the absorption generated by the ion exchange is the most efficient and economic (El-Eswed, 2019). Zeolites are widely used in ion-exchange applications, as they exchange cations from their structure with dissolved ones (Inglezakis, 2005). For this reason, they are used for purification of textile wastewater from basic dyes (Meshko et al, 2001; Akgul et al, 2011; Wang et al, 2006).

In the last few years geopolymers have been studied for a wide range of uses in chemical engineering, such catalysis (Sazama et al, 2011; Alzeer et al, 2018), adsorption/separation of CO_2 (Minelli et al, 2016; Minelli et al 2018), pH-buffering (Ascensão et al, 2017; Novais et al, 2017) and water purification from heavy metals and dyes (El-Eswed, 2019; Li et al, 2006; Zhang et al, 2013a; Siyala et al, 2018; Ge et al 2017; Hua et al, 2020). Furthermore, Zhang et al. (Zhang et al., 2013b) reported the use of fly-ash based geopolymers as photocatalysts for the degradation of

methylene blue, thanks to the presence of Fe_2O_3 and TiO_2 impurities that, under UV irradiation, allow the oxidation of the cations of the adsorbed dye by hydroxyl radicals.

Bortnovsky (Bortnovsky et al, 2008) and Davidovits (Davidovits, 2008) defined geopolymers as the amorphous equivalent or precursor of zeolites. In details, the final microstructure of geopolymers is micro-meso-porous (Kriven et al, 2013; Landi et al, 2013), while the amorphous network, consisting of an alternating sequence of tetrahedral [SiO_4] and [AlO_4]- balanced by alkali cations, endows the geopolymer matrix with ion-exchange properties similar to that of zeolites (Bortonovsky et al, 2008).

Geopolymers are alkali-aluminosilicates synthetized at a temperature below 100 °C from aluminosilicate powders and alkaline aqueous solutions (Davidovits, 2008). Being the synthesis of geopolymers easier and with lower energy and water demand than that of zeolites, they can be directly formulated at low temperature also in spherical shape (El-Eswed, 2019, Ascensão et al, 2017; Novais et al, 2017; Li et al, 2006; Zhang et al, 2013a; Siyala et al, 2018; Medri et al, 2020). In fact, the use of spheres can enhance the bulk adsorption capacity in comparison with the use of monolith, together with facilitating the separation steps when compared to powders (Novais et al, 2019). Different dripping techniques such as injection and solidification methods in PEG (Novais et al, 2017; Li et al, 2006; Medri et al, 2020; Novais et al, 2019; Ge et al, 2015; Tang et al, 2015) or liquid N_2 (Medri et al, 2020; Papa et al, 2019; Papa et al., 2020) as well ionotropic gelation (alginate in $CaCl_2$) (Ge et al, 2017; Medri et al, 2020) have been already tested for the production of geopolymer spheres by using different raw materials, compositions and stoichiometry.

In this study geopolymer spheres produced from a same slurry by different dripping techniques (Medri et al, 2020) are investigated to evaluate the effects of the spheres' morphology and composition on both their mechanical strength and adsorption properties using a positively charged dye (methylene blue) as a cationic model dye.

2. Materials and methods

2.1. Preparation of the geopolymer spheres

Metakaolin Argical™ M1200S from Imerys (SSA= 25 m^2 g^{-1}, d50= 1.5 μm) was used as aluminosilicate powder. Chemical and mineralogical compositions of Argical™ M1200S are detailed elsewhere (Medri et al, 2010; Medri et al. 2020). Potassium di-silicate solutions with molar ratios H_2O:K_2O = 13.5 or 16.0 and SiO_2:K_2O = 2.0 were used as alkaline aqueous solutions (Medri et al. 2020).

Geopolymer slurries with a theoretical molar ratios SiO_2:Al_2O_3 = 4 (Medri et al, 2020) and K_2O:Al_2O_3 = 0.8 were prepared by mixing at 900 rpm metakaolin with potassium di-silicate solutions, using a planetary centrifugal mixer (THINKY MIXER ARE-500) at room temperature.

Geopolymer spheres were prepared by three different dripping techniques (Medri et al, 2020):

i) injection - solidification method in PEG2000 (Merck) at 60 °C of a geopolymer mixture prepared using a potassium di-silicate solution with a molar ratio H_2O:K_2O= 16.0 (here coded G16PEG). The formed spheres were then collected and washed in hot water for PEG removal.

ii) Injection - solidification method in liquid nitrogen of a geopolymer mixture prepared using a potassium di-silicate solution with a molar ratio H_2O:K_2O= 13.5, that after a first maturation step at room temperature was added with distilled water (50 vol.% over the theoretical volume of the geopolymer solid matrix plus the added water). After freezing in liquid N_2, the spheres (coded G13LN) were collected in a freeze dryer set at −40 °C (Edwards Mod.MFD01, Crawley, UK), where the ice was sublimated (-40 °C /+25 °C, P= $8 \cdot 10^{-2}$ torr).

iii) Ionotropic gelation of a geopolymer slurry prepared using a potassium di-silicate solution with a molar ratio H_2O:K_2O= 13.5 blended with a 4 wt.% of sodium alginate (Aldrich) solution (geopolymer/Na-alginate dry weight ratio equal to 4). A modified formulation was obtained by adding up to 20 wt.% of TiO_2 P25 (SSA= 50 m^2g^{-1}, d50 =

20 nm, Degussa) as a photocatalytic secondary phase. The used amount of 20 wt.% was the highest that could be added to the slurry avoiding the blockage of the nozzle, in accordance with the dripping technique. The mixed slurry was added dropwise in a $CaCl_2 \cdot 2H_2O$ (Merck) solution (0.5 M) at 45 °C. The hybrid spheres (coded G13A or G13A-20TiO_2 when TiO_2 was added) were kept in $CaCl_2$ solution for 30 min and then washed in hot water.

Standardized final treatments were applied. To complete the processes, all the spheres were put in a heater for 24 h at 60 °C and finally rinsed in deionized water for 24 h and dried at 60 °C.

Table 1 resumes the prepared samples, coded on the basis of the different dilution (molar ratio H_2O:K_2O) of the potassium di-silicate solutions and the used bath.

2.5 Characterisation

The morphological and macrostructural features of the geopolymer spheres were investigated by digital microscopy (3D Digital Microscope RH2000, Hirox, Japan). Environmental Scanning Electron Microscope (E-SEM FEI Quanta 200) was used to study the microstructure of samples previously gold coated by using a turbo-pumped sputter coater (Quorum Q150T ES).

The pore size distribution of the spheres, in the range 0.0058-100 μm, was analyzed by mercury intrusion porosimetry (MIP Thermo Finnigan Pascal 140 and Thermo Finnigan Pascal 240). The experimental error of the method was 4%. The specific surface area of the spheres was calculated by the Brunauer-Emmett-Teller (BET) method, by means of nitrogen adsorption at 77 K in a Thermo Scientific™ Surfer instrument. The experimental error of this measurement was 1%.

The elemental compositions of the spheres were determined by X-Ray Fluorescence (XRF) analysis on powdered material. Measurements were performed by X-MET7500 Mining Analyser (Oxford Instruments) equipped with Mining_LE_FP (standardless Fundamentl Parameter Calibration).

Compressive strength was determined following ISO 18591:2015, that specifies the testing method to define the compressive strength of ceramic granules when subjected to uniaxial compressive

loading in a confining die. Compressive strength tests were performed at room temperature using a testing machine (Zwick Z050, loading cell class 05, GmbH, Ulm, Germany) and a cross-head speed of 1 mm min^{-1}. The cylindrical die, made of hardened steel, had a 12 mm internal diameter, a 50 mm external diameter and height of 60 mm. The mechanical tests were repeated 4 times for each type of spheres.

In order to determine the adsorption efficiency of the geopolymer spheres, the evolution of the concentration of methylene blue (MB) in aqueous solution was analysed by means of a LAMBDA 750 UV/Vis/NIR Spectrophotometer, PerkinElmer. The wavelength used for the MB was 664 nm. 100 mL of the dye aqueous solution, with a concentration between 10 ppm and 500 ppm, were put in a beaker with 1 g of spheres. Then, the solution was placed under mild magnetic stirring. After periodic intervals, the solution was collected and analyzed. According to the concentration of the solution, the sample was diluted to meet the instrument's measurement range (< 10 ppm). Furthermore, the photodegradation of a 10 ppm MB solution was investigated on a G13A composition with 20 vol.% TiO_2 (G13A-20TiO_2, Table 1). The solution (100 mL) was magnetically stirred and placed in the dark for 30 min to establish an adsorption/desorption equilibrium with the spheres (1 g), then it was irradiated by a UV-lamp (Osram Ultra Vitalux 300 W) and analyzed.

3. Results and discussion

3.1. Geopolymer spheres characterization

3.1.1 Morphological and textural characterization

A description of the morphological and textural characteristics of the spheres produced by the three dripping techniques is given in the following. Fig. 1 reports digital microscope images of the spheres, while Table 2 resumes the main textural properties and Fig. 2 shows the pore size distributions, where the pores in the range 5–50 nm account for the intrinsic mesoporosity of geopolymer matrix (Landi et al, 2013).

155 In the case of the injection - solidification method in PEG, uniform and integer beads with spherical
156 shape were obtained (Fig. 1a, d) due to the surface tension at the liquid/liquid interface and PEG's
157 hydrophilicity and density (Tang et al, 2015). Using PEG2000, the process temperature had to be
158 set at 60 °C to reach a high number of intact spheres (Medri et al, 2020). The low values of SSA and
159 total pore volume were congruent with the high density of the spheres (Table 2) while the bimodal
160 pore size distribution had the main peak centered at 0.5 μm (Fig. 2a).
161 Concerning injection - solidification in liquid nitrogen, spheres (Fig. 1b) were obtained as the drops
162 interacted with liquid nitrogen following the "inverse" Leidenfrost effect (Adda-Bedia et al, 2016).
163 Drops levitated since a vapor layer was formed when heat passed from drops to the bath of liquid
164 nitrogen (Adda-Bedia et al, 2016). After ice sublimation, radial pores and radial cracks were present
165 in the cross section of the spheres (Fig. 1e) as the result of a directional freezing (and consequently
166 ice growth) from the outer surface of the spheres towards the center. Spheres dripped in liquid
167 nitrogen showed the highest mean diameter, open porosity, specific surface area and the lowest bulk
168 density (Table 2) because they were produced by an indirect foaming method (Studart et al., 2006)
169 such a sacrificial template method, where the ice formation templates the porous structure, the so-
170 called ice-templating (Deville et al, 2007; Deville, 2008; Li et al, 2012). Also in this case, a bimodal
171 pore size distribution was obtained (Fig. 2b) with the main peak located at 2-3 μm since
172 interconnected pores of these dimensions were also formed due to ice segregation (Medri et al.,
173 2020; Papa et al., 2020).
174 Finally in ionotropic gelation (Giri et al, 2013), due to the capability of sodium alginate to gel
175 immediately when coming in contact with multivalent cations, geopolymer/ Ca-alginate hybrid
176 spheres were formed by dripping the geopolymer slurry mixed with sodium alginate in a $CaCl_2$ bath
177 (Davarci et al, 2017). These hybrid spheres looked like a "golf ball" (Fig. 1c) because of the
178 formation of a worm-like Ca-alginate cage (Medri et al, 2020). The spheres showed a high pore
179 volume due to the presence of alginate, but low specific surface area (Table 2) and their small size
180 was due to the shrinkage caused by the evaporation of water during the drying process (Medri et al,

2020). Size, pore volume and specific surface area increased in G13A-20TiO_2, owing to the addition of nanometric TiO_2. A monomodal pore size distribution (Fig. 2d, e), likely due to the drying shrinkage, was maintained also when TiO_2 was added to the composition.

3.1.2 Chemical composition

The final content of K and Si in the spheres is strictly linked to the dripping technique (Table 3). In fact, the geopolymer slurry contains a potassium silicate aqueous solution that continuously modifies its chemical composition during the geopolymerization and interacts with the different baths.

In the case of injection-solidification in PEG, the molar ratio SiO_2:Al_2O_3 was slightly lower than expected, while K_2O:Al_2O_3 molar ratio slightly increased due to a partial de-mixing and diffusion of aqueous silicate in the PEG bath.

Concerning injection-solidification in liquid nitrogen, both SiO_2:Al_2O_3 and K_2O:Al_2O_3 were quite lower than the theoretical ones. The potassium silicate solution is as a polymer solution of silicate oligomers, stabilized by K_2O (i.e. KOH:H_2O) (Hunt et al, 2011). In liquid nitrogen, the water started to crystallize into ice leaving the residual water over-saturated with respect to SiO_2. Due to the fast freezing of the drops, the development of large chains of silicate oligomers was quenched (Papa et al, 2015): the silicate remained partially entrapped within the ice crystals, together with the soluble K_2O that was then washed away during the rinsing step. The composition of the salt removed by the final water rinsing was roughly estimated as $K_2O{\cdot}1.4SiO_2$, with a slightly lower amount of silicate in respect to potassium di-silicate ($K_2O{\cdot}2SiO_2$). It follows that the discrepancy in the SiO_2:Al_2O_3 and K_2O:Al_2O_3 molar ratios was due to the fast freezing in liquid nitrogen that stopped the geopolymerization reaction.

Regarding hybrid spheres, being sodium alginate ($C_6H_9NaO_7$) added in the amount of 0.6 moles over the geopolymer slurry composition, it could be assumed that max 0.3 moles of calcium were engaged in forming Ca-alginate. However, XRF results in Table 3 suggested that additional Ca^{2+}

from $CaCl_2$ bath almost completely substituted K^+ in the geopolymer network, since a ionic exchange occurred due to the smaller size of the Ca^{2+} cation (low hydration radius), its high charge and its presence in large excess. Furthermore, the calculated molar ratio $(2CaO+K_2O):Al_2O_3$ was equal to 1.3±0.1, with a further excess of Ca^{2+} and K^+ attributable to impurities in raw materials and probably to carbonates.

3.1.3 Mechanical properties

The method reported in the ISO 18591 standard was used to determine the compressive strength of the geopolymer spheres. In fact, granules rearrange themselves for maximum packaging when compacted in a limited space, such as a die. However, granules deform and fracture when critical pressure P_c is exceeded and the final density of the compact depends on the critical pressure, namely the compressive strength of the granules. When the granules are pressed into a die using a universal material testing machine, the obtained load-displacement curve can be converted into a pressure-density curve by using the dimensions and density of the compact in the following Equation:

$$\rho_p = \frac{m}{V} = \frac{m}{\{Ax[h + (l_f - l]\}} \quad (1)$$

where ρ_p is density, m the mass, V the volume, A the base area and h the height of the die-pressed compact; l_f is overall displacement of the piston while l is displacement of the piston over time.

Fig. 3 shows the load - displacement and pressure - density diagrams of the three types of spheres, while Table 4 reports the obtained critical pressure P_c and density values. G13A had a greater compressive strength than the other samples thanks to the Ca-alginate skeleton, while G13LN showed the lowest Pc because of the high porosity (Papa et al., 2020). It should be noted that in the case of G13A and G13LN, the density of the compact determined by the slope intercept is the same as that of the spheres (in the limit of the experimental error, Table 2), while in the case of G16PEG

232 it is slightly lower due to superficial microcracks that act as critical flaws (Fig. 4), thus decreasing
233 the strength.
234
235 **3.2. Methylene blue adsorption tests**
236 **3.2.1 Influence of methylene blue concentration**
237 The spheres were characterized by adsorption of a cationic model dye, namely methylene blue. The
238 adsorption mechanism is based on the ionic exchange between the counter-cation of the geopolymer
239 (K^+ or Ca^{2+}) and the MB.
240 To assess the adsorption difference between the various samples, the removal efficiency "q" and the
241 percentage of adsorption "E%" were used, being:
242 $$q = \frac{C_0 - C_t}{m} \cdot V = \left[\frac{mg}{g}\right] \quad (2)$$
243 $$E\% = \frac{C_0 - C_t}{C_0} \cdot 100 \quad (3)$$
244
245 where C_0 and C_t (mg L^{-1}) are the initial and time t concentrations, respectively; V (L) is the volume
246 of the solution, and m (g) is the adsorbent dosage.
247 The results are shown in Fig. 5 and Table 5. By using a MB concentration of 10 ppm, G13LN
248 sample had a much more effective adsorption than the other samples, while G16PEG and G13A
249 samples showed a similar trend. This can be explained by the different porosities of the materials:
250 the high porosity of G13LN allowed MB to permeate more rapidly, while the high specific surface
251 area maximized the ion exchange. The images of the three samples after adsorption (Fig. 6a-c)
252 show how G13A and G16PEG samples were completely saturated, while G13LN adsorbed the dye
253 mainly on its surface. Therefore, it can be assumed that the G13LN sample could absorb more dye
254 per gram of material and that the adsorption was limited due to the depletion of the dye in the
255 solution. When a solution of MB at 50 ppm was used, a similar trend was observed (Fig. 5c, d and
256 Fig. 6d-f), with a significantly higher adsorption by G13LN sample, which had not yet reached its
257 adsorption limit (Fig. 6f). The sample saturation occurred only when a 500 ppm solution was used

(Fig. 6g). Also the sample composition influenced the efficiency of ion exchange, since a higher amount of $[AlO_4]^-$ allows a better adsorption by ion exchange, therefore a high degree of geopolymerization should lead to a high ion exchange. In the case of G13A, despite the Ca-alginate adsorption properties (Li et al, 2017), the amount of geopolymer available for ionic exchange is lower than that in the other samples: values of q equal to 0.96 and 4.2 mg g^{-1} and E% equal to 97 and 82 were recalculated over the geopolymer phase weight, respectively for 10 ppm and 50 ppm MB.

3.2.2 Adsorption kinetics

To study the adsorption kinetics of MB on geopolymer spheres, the experimental data from Fig. 5 were fitted into a linear function for the sorption of liquid-solid systems by the pseudo-first-order rate Equation (4) (Lagergren, 1898), the pseudo-second-order rate Equation (5) (Ho et al, 1999) and intraparticle diffusion rate Equation (6) (Crank, 1933):

$$\log (q_e - q_t) = \log q_e - \frac{k_1}{2.303} \cdot t \quad (4)$$

$$\frac{1}{q_t} = \frac{1}{k_1 q_e^2} + \frac{1}{q_e} \cdot t \quad (5)$$

$$q_t = k_p x\, t^{1/2} + c \quad (6)$$

where q_e (mg g^{-1}) and q_t (mg g^{-1}) are the removal efficiencies of the dye at equilibrium and at a time t, respectively, k_1 (min^{-1}) is the first-order rate constant, k_2 (g·(mg min)$^{-1}$) is the second-order rate constant and k_p is the intra-particle diffusion rate constant (mg·(g $min^{1/2}$)$^{-1}$).

As already observed (Zhang et al, 2013; Novais et al, 2019; Papa et al., 2020) the values of correlation coefficients (R^2) (Table 6) confirm that the experimental data of the adsorption kinetics of MB on geopolymers fit with the pseudo-second-order rate equation which points out the nature of the ion exchange process. In particular, for G13LN, R^2 is up to 0.999 and q_e is close to the removal efficiency q (Table 5). Also in the case of G13A, a very good correlation with the second order kinetics is maintained since the adsorption process on Ca-alginate as well follows the pseudo-

second-order reaction model (Li et al, 2017). However, in the case of G16PEG with a 10 ppm MB solution, R^2 is equal to 0.98 for both the pseudo-second-order rate and intraparticle diffusion rate equations, suggesting that, at low dye concentrations, both processes can be rate-determining steps, probably due to the very low open porosity of these spheres (29%, Table 2). Instead, at 50 ppm of concentration, R^2 is equal to 0.99 for both the pseudo-first-order rate and pseudo-second-order rate equations, suggesting as for this type of spheres MB adsorption is a more complex process.

3.2.3 UV irradiation of TiO_2 composite spheres

TiO_2 P25 has been added to the geopolymer as a photocatalytic additive to increase the amount of dye removal from the solution. In particular, MB, in the presence of TiO_2, degrades in CO_2, NH_4^+, NO_3^-, SO_4^{2-} (Houas et al, 2001). Since ionotropic gelation allows the addition of a secondary phase more easily than the other dripping methods, due to the mechanism of gelation that stabilizes the composite mixtures, G13A-20TiO_2 was prepared and the photodegradation of a 10 ppm MB solution was investigated.

The effect of UV irradiation is show in Fig. 7. Already after 50 minutes of test (20 minutes of irradiation) the curves of the sample subjected to UV radiation and of the untreated sample started to diverge. Furthermore, after 120 minutes q was equal to 0.56 and 0.42 mg g^{-1}, while E% was 52 and 41 respectively with and without UV irradiation. It should be pointed out that in the case of untreated G13A (Fig. 5a, b), besides a faster removal rate in the first 15 minutes of test, after 120 minutes q was only 0.39 mg g^{-1} and E% was 39. The efficacy of TiO_2 can be therefore confirmed as an effective photocatalytic filler for geopolymer-based spheres for the degradation of MB.

4. Conclusion

The research was aimed at verifying mechanical and absorption properties of metakaolin based geopolymer spheres of millimetric size, produced with three different dripping methods: injection

and consolidation in polyethylene glycol bath (PEG) and in liquid nitrogen (ice-templating), and ionotropic gelation.

The characteristics of the spheres depend on the production process. The total porosity increased in the order G16PEG<< G13A< G13LN, while the specific surface is G16PEG ≈ G13A << G13LN respectively. The different chemical composition given by the three dripping methods was mainly caused by:

- a partial de-mixing and diffusion of the aqueous silicate in the hydrophilic PEG for G16PEG;
- rapid freezing, which stops the geopolymerization, decreasing both SiO_2:Al_2O_3 and K_2O:Al_2O_3 ratios for G13LN.
- the presence of Ca^{2+} from the $CaCl_2$ bath that leads to an almost complete substitution of the K^+ counter-cation, as regards the spheres obtained by ionotropic gelation (G13A).

Porosity and composition influenced the mechanical properties of the spheres. In fact, the hybrid sample G13A was the one with the greatest compressive strength, 18.7 MPa, thanks to the presence of the Ca-alginate skeleton. G16PEG sample, on the other hand, had a slightly lower resistance, 12.9 MPa, due to the presence of superficial micro-fractures. Finally, due to their high porosity, G13LN spheres had a much lower compressive strength of 3.3 MPa.

The absorption of cationic dyes, such as MB, occurred via ion-exchange mechanism, an intrinsic property of the geopolymer itself. The highest removal efficiency and adsorption percentage were observed for G13LN. All geopolymer spheres were consistent with the pseudo-second-order adsorption equation, but G16PEG, depending on MB concentration, also fitted with intraparticle diffusion rate and pseudo-first-order equations.

Finally, spheres produced by ionotropic gelation and added with 20 vol.% TiO_2 exhibited an increase of removal efficiency of 33% after 90 minutes of UV irradiation, highlighting the possibility of functionalizing and further increasing the performances of this type of geopolymer spheres.

Acknowledgements

The authors greatly thank Mrs Andreana Piancastelli for MIP analyses and Mr Emeric Sauzeau for samples preparation.

Bibliography

Adda-Bedia, M., Kumar, S., Lechenault, F., Moulinet, S., Schillaci, M., Vella, D., 2016. Inverse Leidenfrost Effect: Levitating Drops on Liquid Nitrogen. Langmuir 32, 4179–4188.

Ahmad, R., Guo, J., Kim, J., 2019. Structural characteristics of hazardous organic dyes and relationship between membrane fouling and organic removal efficiency in fluidized ceramic membrane reactor, J. Clean. Prod. 232, 608-616.

Akgul, M., Karabakan, A., 2011. Promoted dye adsorption performance over desilicated natural zeolite, Microporous Mesoporous Mater. 145, 157–164.

Alzeer, M. I. M., MacKenzie, K. J. D., 2018. Synthesis and catalytic properties of new sustainable aluminosilicate heterogeneous catalysts derived from fly ash. ACS Sustainable Chem. Eng. 6, 5273−5282.

Ascensão G., Seabra, M.P., Aguiar, J.B., Labrincha, J.A., 2017. Red mud-based geopolymers with tailored alkali diffusion properties and pH buffering ability. J. Clean. Prod. 148, 23-30.

Bortnovsky, O., Dedecek, J., Tvaruzkova, Z., Sobalík, Z., Subrt, J., 2008. Metal ions as probes for characterization of geopolymer materials. J. Am. Ceram. Soc. 91, 3052-3057.

Boyd, G.E., Adamson, A.W., Myers Jr, L.S., 1947. The exchange adsorption of ions from aqueous solutions by organic zeolites. II. Kinetics1, J. Am. Chem. Soc. 69, 2836-2848.

Crank, G., 1933. The mathematics of diffusion, London, New York: Clarendon Press.

Davarci, F., Turan, D., Ozcelik, B., Poncelet, D., 2017. The influence of solution viscosities and surface tension on calcium-alginate microbead formation using dripping technique. Food Hydrocoll. 62, 119-127.

Davidovits, J., 2008. Geopolymers Chemistry and Applications, Institut Geopolymere: Saint-Quentin, France.

Deville, S., Saiz, E., Tomsia, A.P., 2007. Ice-templated porous alumina structures. Acta Mater. 55, 1965–1974.

Deville, S., 2008. Freeze-casting of porous ceramics: A review of current achievements and issues. Adv. Eng. Mater. 10, 155–169.

El-Eswed, B.I., 2019. Aluminosilicate inorganic polymers (geopolymers): emerging ion exchangers for removal of metal ions, in: Inamuddin, M. Ahamed, A. Asiri (Eds.), Applications of ion exchange materials in the environment, Springer Nature Switzerland AG, pp. 65-94.

Ge, Y., Cui, X., Kong, Y., Li, Z., He, Y., Zhou, Q., 2015. Porous geopolymeric spheres for removal of Cu(II) from aqueous solution: synthesis and evaluation. J. Hazard. Mater. 283, 244–25.

Ge, Y., Cui, X., Liao, C., Li, Z., 2017. Facile fabrication of green geopolymer/alginate hybrid spheres for efficient removal of Cu(II) in water: batch and column studies. Chem. Eng. J. 311, 126–134.

Giri, T.K., Verma, S., Alexander, A., Ajazuddin, A., Badwaik, H., Tripathy, M., Tripathi, D.K., 2013. Cross-linked biodegradable alginate hydrogel floating beads for stomach site specific controlled delivery of metronidazole. Farmacia 61, 533-550.

Ho, Y.S., McKay, G., 1999. Pseudo-second order model for sorption processes, Process Biochem. 34, 451–465.

Hua, P., Sellaoui, L., Franco, D., Netto, M.S., Dotto, G.L., Bajahzar, A., Belmabrouk, H., Bonilla-Petriciolet, A., Li, Z., 2020. Adsorption of acid green and procion red on a magnetic geopolymer based adsorbent: Experiments, characterization and theoretical treatment, Chem. Eng. J. 383, 123113.

Houas, A., Lachheb, H., Ksibi, M., Elaloui, E., Guillard, C., Herrmann, J-M., 2001. Photocatalytic degradation pathway of methylene blue in water, App. Catal. B: Environmental 31, 145–157.

386 Hunt, J.D., Kavner, A., Schauble, E.A., Snyder, D., Manning, C.E., 2011. Polymerization of aqueous
387 silica in H_2O–K_2O solutions at 25–200 °C and 1 bar to 20 kbar, Chem. Geol. 283, 161-170.
388 Inglezakis, V.J., 2005. The concept of "capacity" in zeolite ion-exchange systems, J. Colloid
389 Interface Sci. 281, 68–79.
390 Kim, T-H., Park, C., Kim, S., 2005. Water recycling from desalination and purification process of
391 reactive dye manufacturing industry by combined membrane filtration, J. Clean. Prod. 13,
392 779-786.
393 Körbahti, B.K., 2007. Response surface optimization of electrochemical treatment of textile dye
394 wastewater and heat treatments, J. Hazard. Mater. 145, 277–286.
395 Kriven, W.M., Bell, J.L., Gordon, M., 2013. Microstructure and microchemistry of fully-reacted
396 geopolymers and geopolymer matrix composites. Ceram. Trans. 153, 227–250.
397 Lagergren, S.. 1898. Zur theorie der sogenannten adsorption geloster stoffe. Kungliga Svenska
398 Vetenskapsakademiens, Handlingar, 24 (4), 1–39.
399 Landi, E., Medri, V., Papa, E., Dedecek, J., Klein, P., Benito, P., Vaccari, A., 2013. Alkali-bonded
400 ceramics with hierarchical tailored porosity. Appl. Clay Sci. 73, 56–64.
401 Li, L., Wang, S., Zhu, Z., 2006. Geopolymeric adsorbents from fly ash for dye removal from
402 aqueous solution. J. Colloid Interface Sci. 300, 52-59.
403 Li, Q., Li, Y., Ma, X., Du, Q., Sui, K., Wang, D., Wang, C., Li, H., Xi, Y., 2017. Filtration and
404 adsorption properties of porous calcium alginate membrane for methylene blue removal from
405 water, Chem. Eng. J. 316, 623–630.
406 Li, W.L., Lu, K., Walz, J.Y., 2012. Freeze casting of porous materials: Review of critical factors in
407 microstructure evolution. Int. Mater. Rev. 57, 37–60.
408 Liu, C-H., Wu, J -S., Chiu, H-C., Suen, S-Y., Chu, K.H., 2007. Removal of anionic reactive dyes
409 from water using anion exchange membranes as adsorbers, Water Res. 41, 1491–1500.

Medri, V., Fabbri, S., Dedecek, J., Sobalik, Z., Tvaruzkova, Z., Vaccari, A., 2010. Role of the morphology and the dehydroxylation of metakaolins on geopolymerization, App. Clay. Sci. 50, 538–545.

Medri, V., Papa, E., Lizion, J., Landi, E., 2020. Metakaolin-based geopolymer beads: Production methods and characterization, J. Clean. Prod. 118844.

Meshko, V., Markovska, L., Mincheva, M., Rodrigues, A.E., 2001. Adsorption of basic dyes on granular activated carbon and natural zeolite, Water Res. 35, 3357–3366.

Minelli, M., Medri, V., Papa, E., Miccio, F., Landi, E., Doghieri, F., 2016. Geopolymers as solid adsorbent for CO_2 capture. Chem. Eng. Sci. 148, 267–274.

Minelli, M., Papa, E., Medri, V., Miccio, F., Benito, P., Doghieri, F., Landi, E., 2018. Characterization of novel geopolymer - zeolite composites as solid adsorbents for CO_2 capture. Chem. Eng. J. 341, 505-515.

Novais, R.M., Seabra, M.P., Labrincha, J.A., 2017. Porous geopolymer spheres as novel pH buffering materials. J. Clean. Prod. 143, 1114-1122.

Novais, R.M., Carvalheiras, J., Tobaldi, D.M., Seabra, M.P., Pullar, R.C., Labrincha, J.A., 2019. Synthesis of porous biomass fly ash-based geopolymer spheres for efficient removal of methylene blue from wastewaters. J. Clean. Prod. 207, 350-362.

Papa, E., Medri, V., Benito, P., Vaccari, A., Bugani, S., Jaroszewicz, J., Swieszkowski, W., Landi, E., 2015. Synthesis of porous hierarchical geopolymer monoliths by ice-templating. Microporous Mesoporous Mater. 215, 206-214.

Papa, E., Medri, V., Natali Murri, A., Miccio, F., Landi, E., 2019. Ice-templated geopolymer—Fe/Mn oxide composites conceived as oxygen carriers. Ceramics 2, 148–160.

Papa, E., Mor, M., Natali Murri, A., Landi, E., Medri, V., 2020. Ice-templated geopolymer beads for dye removal, J. Colloid. Interf. Sci. 57, 364-373.

Pereira, L., Alves, M., 2012. Dyes—Environmental Impact and Remediation, in: A. Malik, E. Grohmann (Eds.), Environmental Protection Strategies for Sustainable Development. Strategies for Sustainability, Springer, Dordrecht, pp. 111-162.

Rawat, D., Mishra, V., Sharma, R.S., 2016. Detoxification of azo dyes in the context of environmental processes, Chemosphere 155, 591-605.

Sazama, P., Bortnovsky, O., Dědeček, J., Tvarůžková, Z., Sobalik, Z., 2011. Geopolymer based catalysts-New group of catalytic materials. Catal. Today 164, 92-99.

Siyala, A.A., Shamsuddina, M.R., Khana, M.I., Rabata, N.E., Zulfiqara, M., Mana, Z., Siamec, J., Azizli, K.A., 2018. A review on geopolymers as emerging materials for the adsorption of heavy metals and dyes. J. Environ. Manage. 224, 327–339.

Shen, C., Pan, Y., Wu, D., Liu, Y., Ma, C., Li, F., Ma, H., Zhang, Y., 2019. A crosslinking-induced precipitation process for the simultaneous removal of poly(vinyl alcohol) and reactive dye: The importance of covalent bond forming and magnesium coagulation, Chem. Eng. J. 374, 904-913.

Studart, A.R., Gonzenbach, U.T., Tervoort, E., Gauckler, L.J., 2006. Processing routes to macroporous ceramics: A Review, J. Am. Ceram. Soc. 89, 1771–1789.

Tan, B.H., Teng, T.T., Mohd Omar A.K., 2000. Removal of dyes and industrial dye wastes by magnesium chloride, Water Res. 34, 597-601.

Tang, Q., Ge, Y., Wang, K., He, Y., Cui, X., 2015. Preparation and characterization of porous metakaolin-based inorganic polymer spheres as an adsorbent. Mater. Design 88, 1244-1249.

Wang, S., Li, H., Xu, L., 2006. Application of zeolite MCM-22 for basic dye removal from wastewater, J. Colloid Interface Sci. 295, 71–78.

Wu, J-S., Liu, C-H., Chu, K.H., Suen, S-Y., 2008. Removal of cationic dye methyl violet 2B from water by cation exchange membranes, J. Membrane Sci. 309, 239–245.

Yaseen, D.A., Scholz, M., 2019. Textile dye wastewater characteristics and constituents of synthetic effluents: a critical review, Int. J. Environ. Sci. Technol. 16, 1193-1226.

Zhang, Y.J., Liu, L.C., Ni, L.L., Wang, B.L., 2013a. A facile and low-cost synthesis of granulated blast furnace slag-based cementitious material coupled with Fe_2O_3 catalyst for treatment of dye wastewater. Appl. Catal. B Environ. 138-139, 9-16.

Zhang, Y., Liu, L., 2013b. Fly ash-based geopolymer as a novel photocatalyst for degradation of dye from wastewater, Particuology 11, 353– 358.

Zhou, Y., Lu, J., Zhou, Y., Liu, Y., 2019. Recent advances for dyes removal using novel adsorbents: A review, Environ. Pollut. 252, 352-365.

Figure captions

Figure 1 Digital microscope images of integer spheres (a,b,c) and cross sections (d,e,f) of G16PEG (a,d), G13LN (b,e) and G13A (c,f).

Figure 2 Pore size distribution by Hg intrusion porosimetry (MIP) of G16PEG (a), G13LN (b), G13A (c) and G13A-20TiO_2 (d).

Figure 3 Load - displacement curves (a) and pressure - density diagrams of G16PEG (a), G13LN (b) and G13A (c), where the slopes are reported as dotted lines.

Figure 4 SEM micrograph showing microcracks on the external surface of a G16PEG sphere.

Figure 5 Influence of contact time on removal efficiency "q" (a,c) and the percentage of adsorption "E%" (b,d) by G16PEG, G13LN and G13A spheres at methylene blue initial concentration of 10 ppm (a,b) and 50 ppm (c,d).

Figure 6 Cross section of G16PEG (a,d), G13LN (b,e,g) and G13A (c,f) spheres after immersion for 24 h in 10 ppm (a,b,c), 50 ppm (d,e,f) and 500 ppm (g) methylene blue solutions.

Figure 7 Effect of UV irradiation on removal efficiency "q" (a) and the percentage of adsorption "E%" (b) by G13A-20TiO_2 spheres at methylene blue initial concentration of 10 ppm and comparison with G13A.

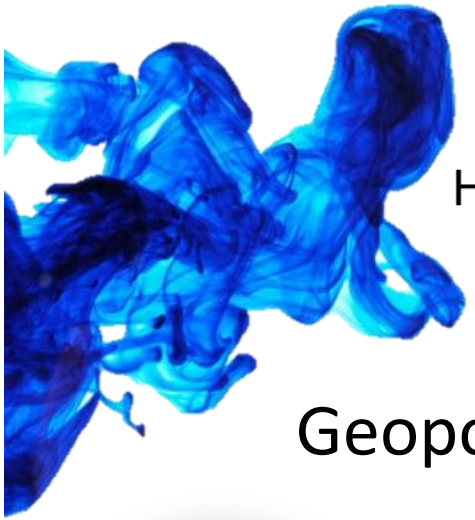

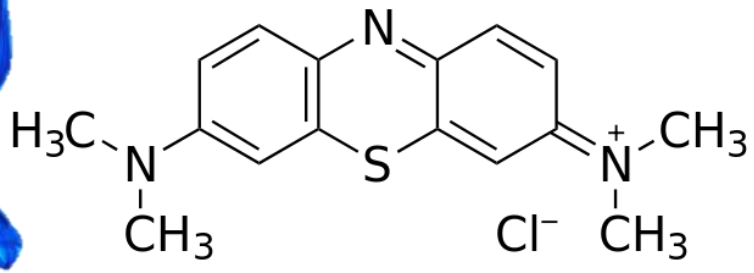

Geopolymer spheres

2mm

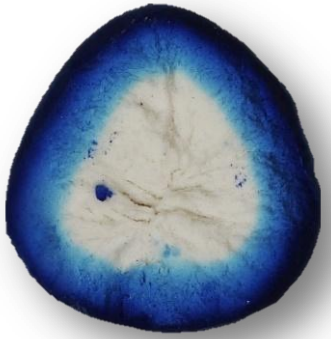

2mm

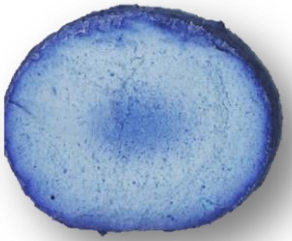

2mm

Highlights:

- Three different dripping techniques were used to produce geopolymer spheres.
- Injection-solidification in PEG, ice-templating and ionotropic gelation were used.
- Porosity varied from 29 % to 66 % and specific surface area from 16 to 63 $m^2 g^{-1}$.
- Compressive strength varied from 3.3 to 18.7 MPa.
- Dye adsorption depended on spheres morphology, porosity and specific surface area.

Table 1. Sample coding.

Sample code	Bath	Geopolymer/ Alginate wt.%	Added H_2O vol.%	TiO_2 vol.%
G16PEG	PEG2000, 60°C	/	/	/
G13LN	Liquid nitrogen	/	50	/
G13A	$CaCl_2$ 0.5M, 45°C	4:1	/	/
G13A-20TiO_2		4:1	/	20

Table 2. Average diameter of the spheres, bulk density and porosity values by mercury intrusion porosimetry (*), BET specific surface area (SSA) by nitrogen adsorption.

Sample	Average diameter (mm)	*Bulk density (g cm^{-3})	*Open porosity (%)	*Total pore volume (mm^3 g^{-1})	*Average pore diameter (µm)	*Modal pore diameter (µm)	SSA (m^2 g^{-1})
G16PEG	2.6 ± 0.1	1.48	29	195	0.05	0.60	16
G13LN	3.2 ± 0.2	0.80	66	824	0.20	2.22	63
G13A (Medri et al, 2020)	2.0 ± 0.1	0.87	59	682	0.14	0.27	16
G13A-20TiO_2	2.3 ± 0.2	0.87	62	714	0.11	0.22	20

Table 3. Elemental composition and molar ratio of the spheres by XRF analysis.

Sample	Si	Al	K	Ca	Fe	Ti	SiO_2:Al_2O_3	K_2O:Al_2O_3
G16PEG	46.37± 0.17	25.30± 0.23	24.69± 0.04	0.21± 0.006	1.87± 0.02	1.55± 0.01	3.67± 0.05	0.98 ±0.01
G13LN	51.22± 0.18	30.73± 0.24	15.09± 0.04	0.12± 0.004	2.20± 0.02	0.63± 0.008	3.33± 0.04	0.49± 0.005
G13A	49.92± 0.55	24.33± 0.63	3.10± 0.02	19.07± 0.22	2.10± 0.24	1.62± 0.04	4.10± 0.15	0.12± 0.004

Table 4. Compressive strength P_c and critical density ρ_c of the various samples obtained according to ISO / DIS 18591.

Sample	**P_c (MPa)**	**ρ_c (g cm^{-3})**
G16PEG	12.9 ± 0.9	1.19±0.06
G13LN	3.3 ± 1.0	0.80±0.03
G13A	18.7 ± 0.9	0.87±0.01

Table 5. The removal efficiency q factor and adsorption percentage E% for samples tested with 10 and 50 ppm of methylene blue after 24 h. In the brackets, the values of q and E% recalculated over the geopolymer phase weight in G13A.

Sample	Methylene blue concentration			
	10 ppm		50 ppm	
	q ($mg\ g^{-1}$)	E%	q ($mg\ g^{-1}$)	E%
G16	0.76	75	3.6	68
G13LN	0.90	94	5.4	98
G13A	0.72 (0.96)	73 (97)	3.2 (4.2)	62 (82)

Table 6. Parameters of kinetics models for the adsorption of methylene blue at different concentration on geopolymer spheres.

Sample	Methylene blue concentration	First order kinetics parameter			Second order kinetics parameter			Intra-particle diffusion parameter	
		k_1 (min^{-1})	q_e (mg g^{-1})	R^2	k_2 (g·(mg min) $^{-1}$)	q_e (mg g^{-1})	R^2	k_p (mg·(g $min^{1/2}$)$^{-1}$	R^2
G16PEG	10 ppm	0.0035	0.6272	0.9428	0.0240	0.6194	0.9825	0.0298	0.9848
	50 ppm	0.0052	3.3986	0.9960	0.0019	3.9479	0.9957	0.1190	0.8074
G13LN	10 ppm	0.0207	0.6616	0.9442	0.0752	0.9117	0.9998	0.0744	0.9304
	50 ppm	0.0099	4.4586	0.9859	0.0045	5.6370	0.9974	0.1696	0.6676
G13A	10 ppm	0.0021	0.5016	0.9674	0.0118	0.7652	0.9948	0.0099	0.9412
	50 ppm	-0.0088	2.4238	0.9727	0.0072	3.2489	0.9999	0.0834	0.5974

Figure 1

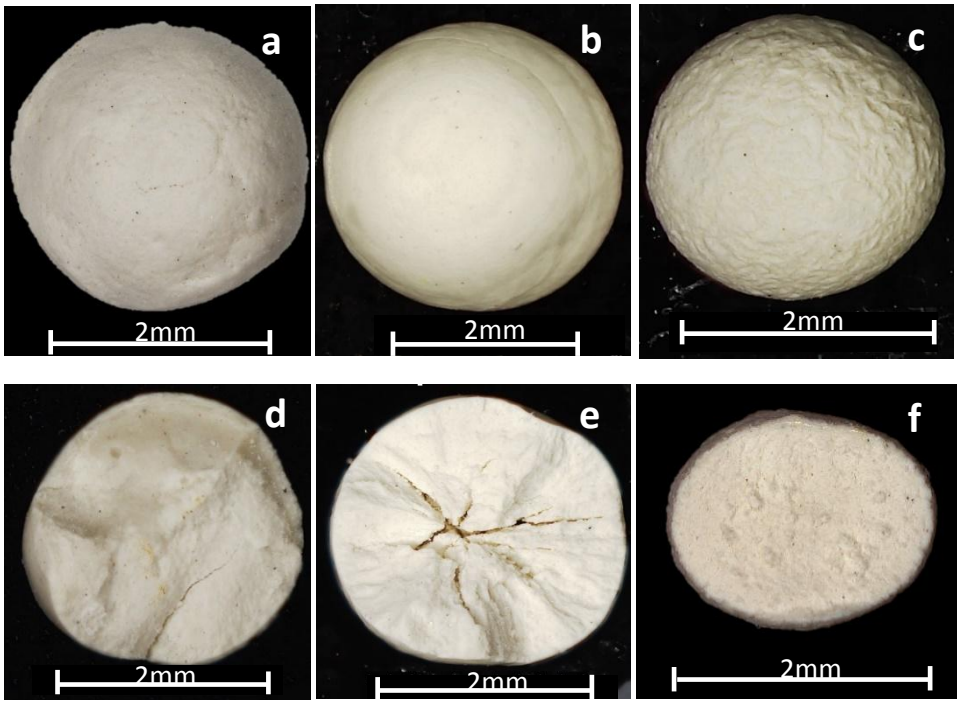

Figure 2

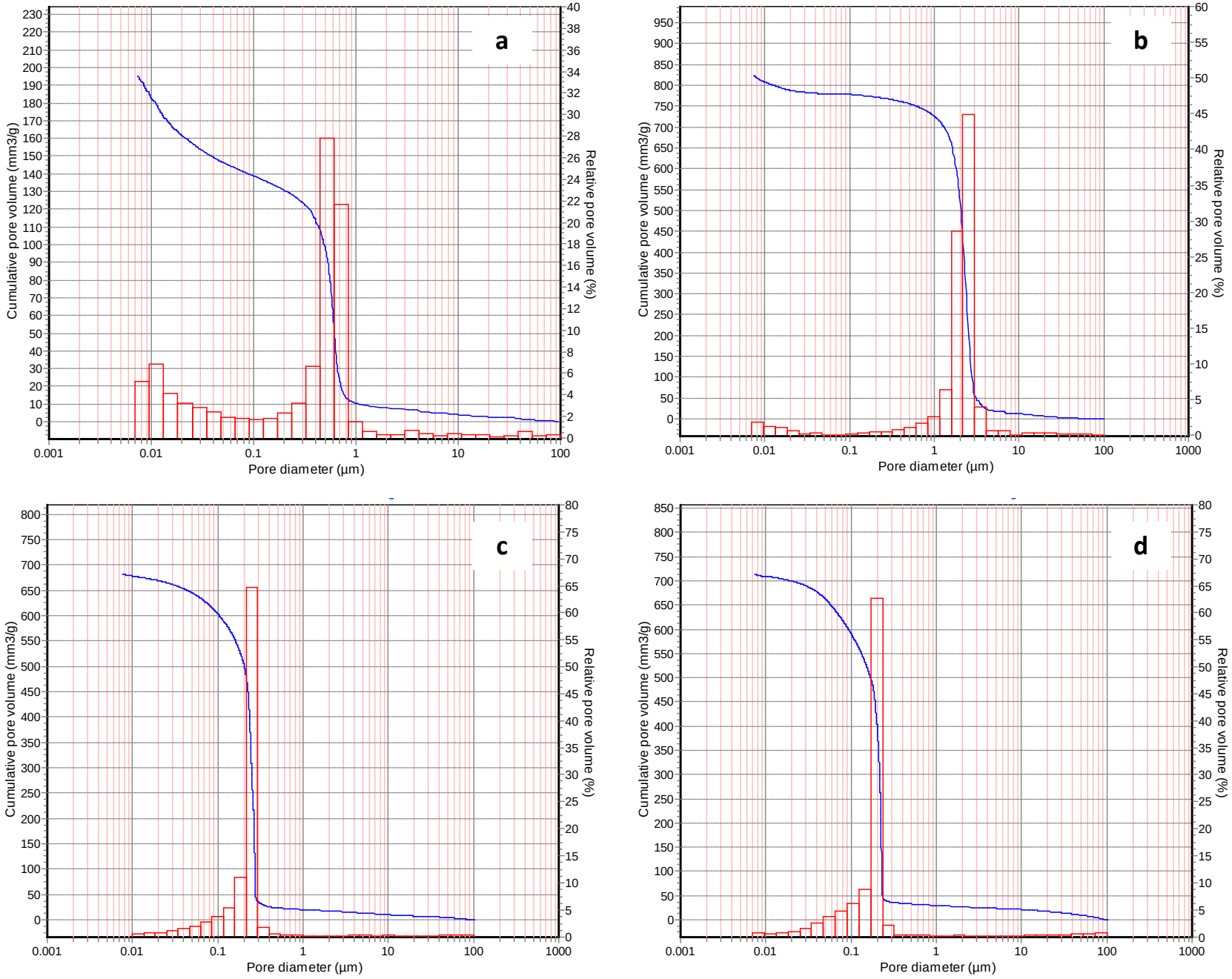
a
b
c
d
Cumulative pore volume (mm3/g)
Relative pore volume (%)
Pore diameter (µm)

Figure 3

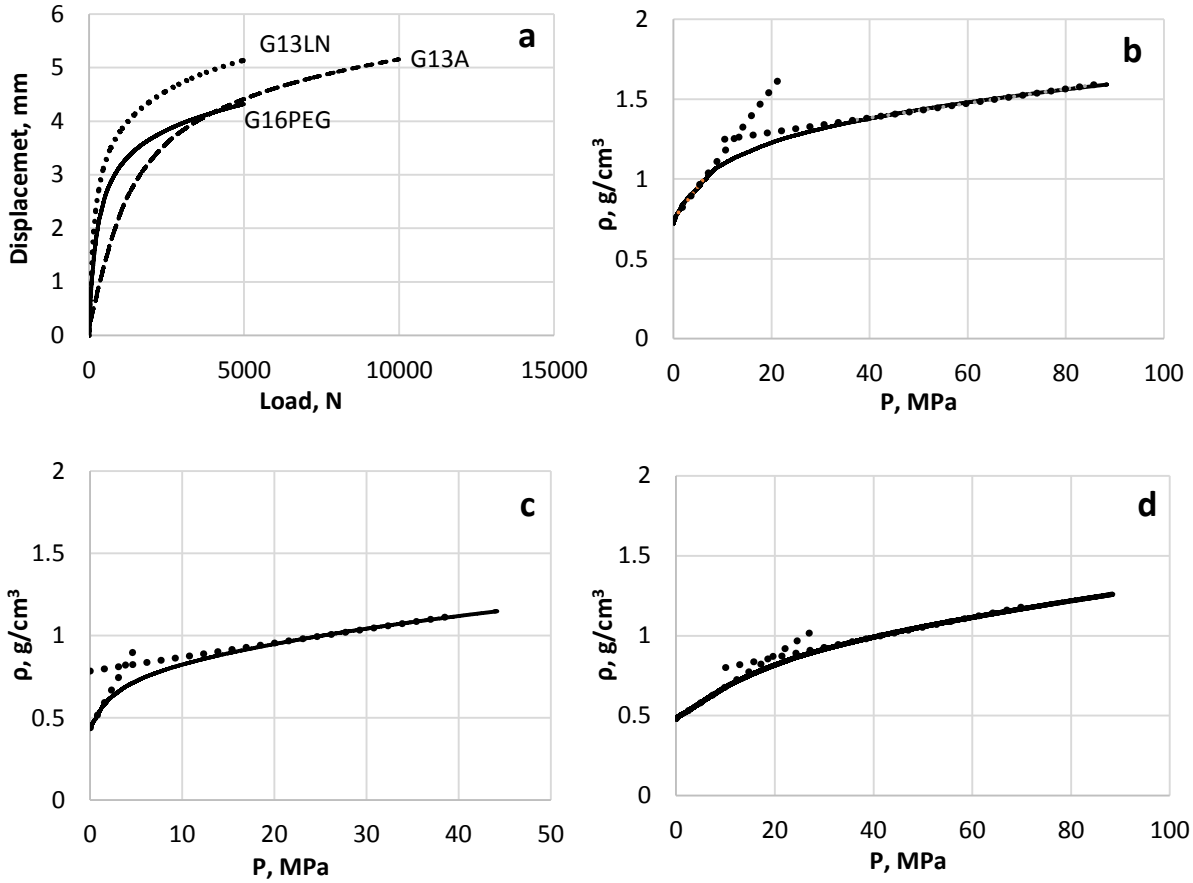
a
G13LN
G13A
G16PEG
Displacemet, mm
Load, N
0
1
2
3
4
5
6
0
5000
10000
15000
b
ρ, g/cm³
P, MPa
0
0.5
1
1.5
2
0
20
40
60
80
100
c
ρ, g/cm³
P, MPa
0
0.5
1
1.5
2
0
10
20
30
40
50
d
ρ, g/cm³
P, MPa
0
0.5
1
1.5
2
0
20
40
60
80
100

Figure 4

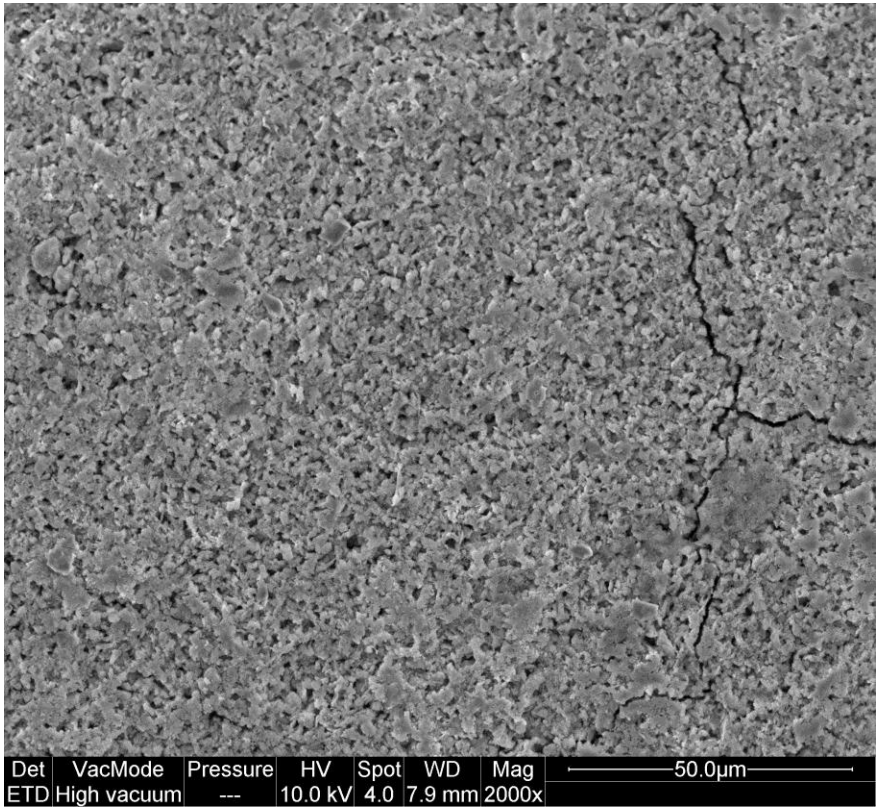
Det ETD
VacMode High vacuum
Pressure ---
HV 10.0 kV
Spot 4.0
WD 7.9 mm
Mag 2000x
50.0µm

Figure 5

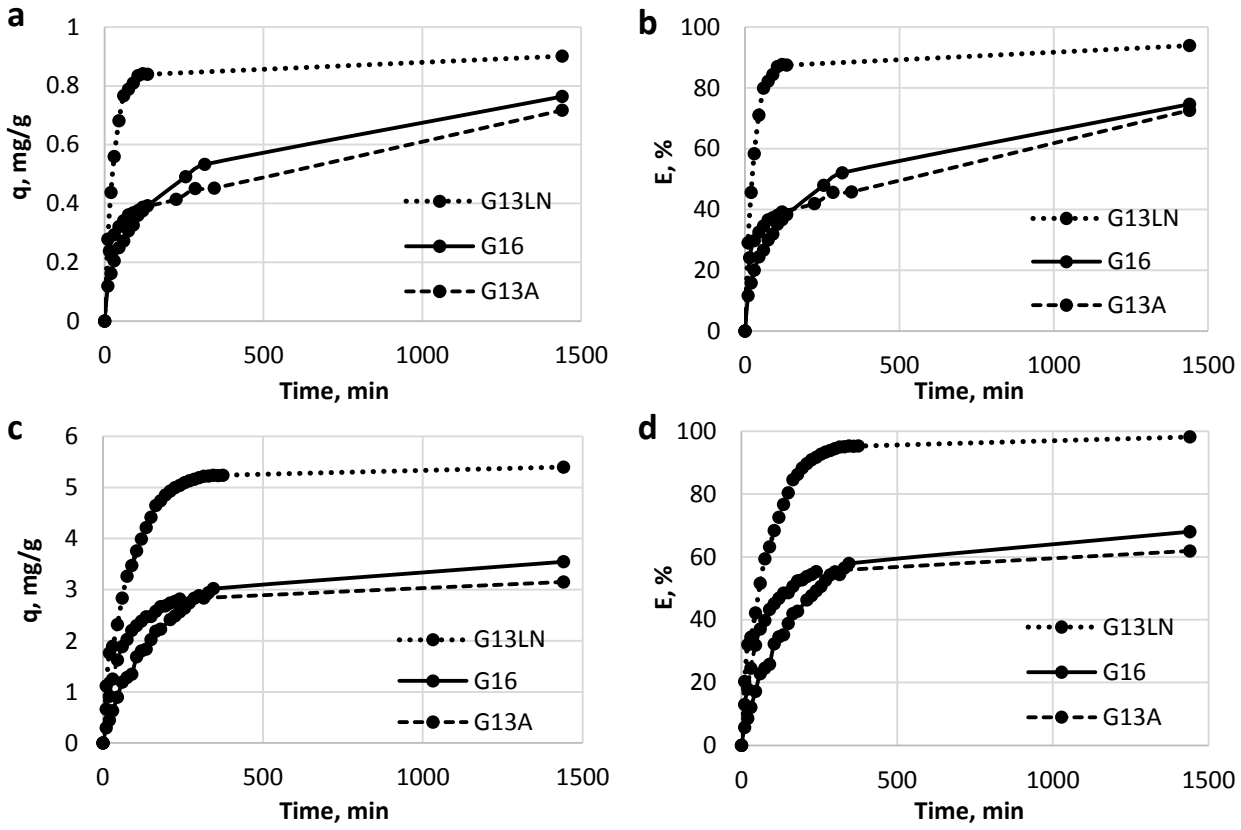
a
q, mg/g
Time, min
G13LN
G16
G13A
b
E, %
Time, min
G13LN
G16
G13A
c
q, mg/g
Time, min
G13LN
G16
G13A
d
E, %
Time, min
G13LN
G16
G13A

Figure 6

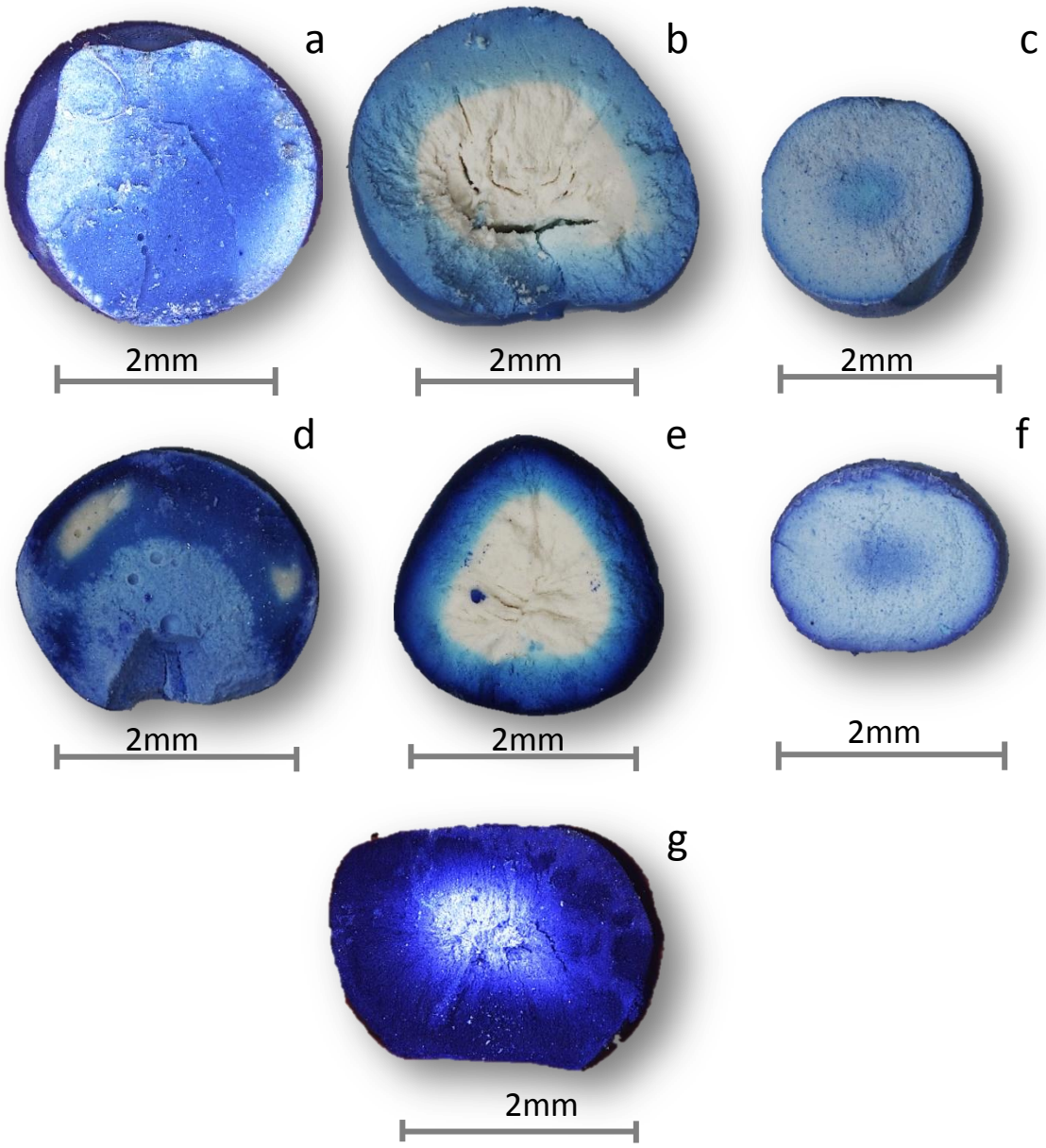

Figure 6

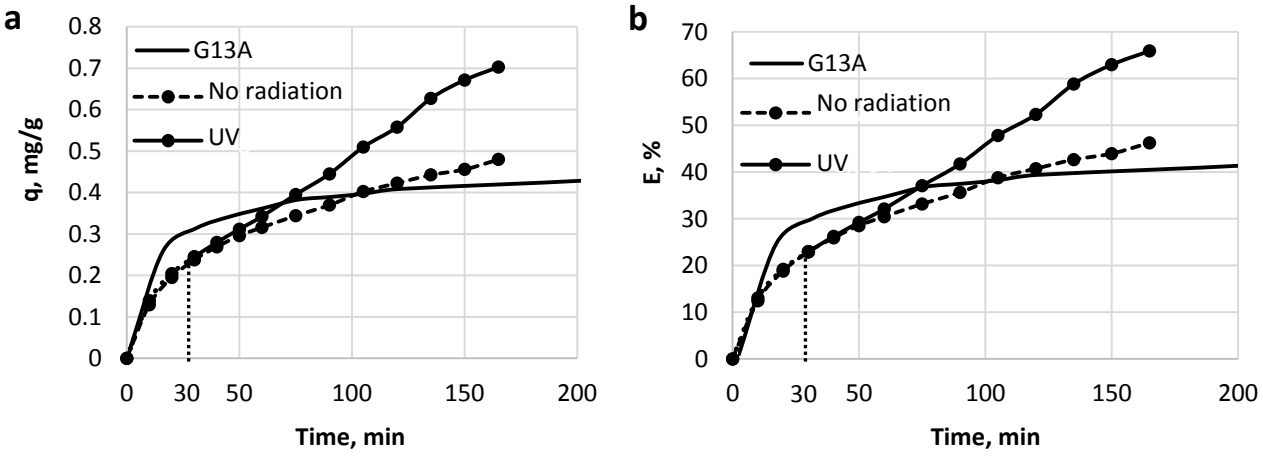
a
q, mg/g
0.8
0.7
0.6
0.5
0.4
0.3
0.2
0.1
0
G13A
No radiation
UV
0
30
50
100
150
200
Time, min
b
E, %
70
60
50
40
30
20
10
0
G13A
No radiation
UV
0
30
50
100
150
200
Time, min